

Robust Tumor Segmentation with Hyperspectral Imaging and Graph Neural Networks

Mayar Lotfy^{1,2}, Anna Alperovich³, Tommaso Giannantonio³, Björn Barz³,
Xiaohan Zhang¹, Felix Holm², Nassir Navab², Felix Boehm⁴,
Carolin Schwamborn⁴, Thomas K. Hoffmann⁴, Patrick J. Schuler⁴

¹Carl Zeiss Meditec AG, Oberkochen, Germany

²CAMP, Technical University of Munich, Garching, Germany

³Carl Zeiss AG, Corporate Research & Technology, Oberkochen, Germany

⁴Dept. of Otorhinolaryngology, University Hospital Ulm, Ulm, Germany

Abstract

Segmenting the boundary between tumor and healthy tissue during surgical cancer resection poses a significant challenge. In recent years, Hyperspectral Imaging (HSI) combined with Machine Learning (ML) has emerged as a promising solution. However, due to the extensive information contained within the spectral domain, most ML approaches primarily classify individual HSI (super-)pixels, or tiles, without taking into account their spatial context. In this paper, we propose an improved methodology that leverages the spatial context of tiles for more robust and smoother segmentation. To address the irregular shapes of tiles, we utilize Graph Neural Networks (GNNs) to propagate context information across neighboring regions. The features for each tile within the graph are extracted using a Convolutional Neural Network (CNN), which is trained simultaneously with the subsequent GNN. Moreover, we incorporate local image quality metrics into the loss function to enhance the training procedure's robustness against low-quality regions in the training images. We demonstrate the superiority of our proposed method using a clinical ex vivo dataset consisting of 51 HSI images from 30 patients. Despite the limited dataset, the GNN-based model significantly outperforms context-agnostic approaches, accurately distinguishing between healthy and tumor tissues, even in images from previously unseen patients. Furthermore, we show that our carefully designed loss function, accounting for local image quality, results in additional improvements. Our findings demonstrate that context-aware GNN algorithms can robustly find tumor demarcations on HSI images, ultimately contributing to better surgery success and patient outcome.

1. Introduction

Head and Neck (H&N) cancer is the sixth most common cancer worldwide [46]. It is located in the upper aerodigestive tract, which comprises the oral and nasal cavities, pharynx, and larynx. The majority of these cancers are squamous cell carcinoma (SCC) and they are often lethal, with a total number of 529,000 new cases yearly resulting in 350,000 cancer-related deaths [15, 16]. Currently, the primary treatment remains surgery, whose outcome is compromised by inadequate cancer margin detection in 10% to 20% of the cases. If residues of cancerous tissue remain, recurrence rates after surgery can be as high as 55% [39].

In the typical surgical workflow, doctors use pre-operative imaging, such as CT or MRI, to plan tumor resection. In addition to that, during the surgical procedure, surgeons rely strongly on prior experience and visual cues, as well as intra-operative pathologist consultations (IPCs) that provide guidance towards the total resection of the cancer tissue. However, IPC is time consuming and may not fully reflect the extent and the delineation of the lesion due to limitations in tissue sampling and preparation. Thus, tumor segmentation solutions based on optical imaging combined with machine learning recently emerged as an attractive addition to the classical pathological testing [65]. This approach holds the promise of non-invasive and real-time tumor segmentation during the surgery.

Hyperspectral imaging (HSI) [7] is an optical modality that combines the benefits of imaging and spectroscopy. It covers a continuous part of the visible (and often IR) spectrum and images the whole field of view at hundreds of narrow wavelength bands, thus recording significantly more information than regular broadband imaging, such as RGB. HSI is an emerging technique in the biomedical laboratory and in the operating room [7, 37], as it is non-invasive, non-

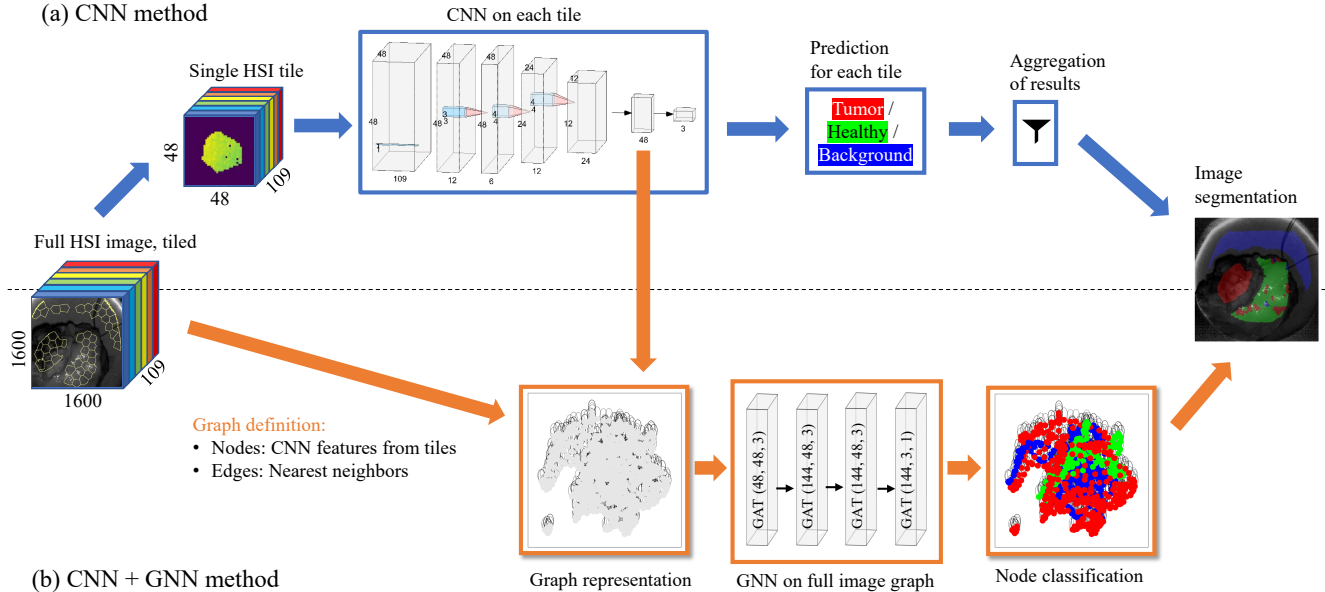


Figure 1. Overview of the segmentation methods we consider. The top section (a, blue arrows) describes the baseline CNN method, while the bottom section (b, orange arrows) represents the CNN+GNN approach. Beginning from the left, we represent the full HSI data cube for one image (the grayscale shows luminosity at a single representative wavelength) with exemplary SLIC tiling overlaid in yellow. The numbers on the x, y, λ axes represent the dimensions. Along the (a) path we show a representative cropped and zero-padded tile, the architecture of the CNN classifier model (each block represents a convolutional layer with feature dimensions at the bottom, spatial dimensions at the left, and kernel dimensions near the blue rectangle), its possible predictions, and their aggregation to image segmentation. Along the (b) path, we show the graph representation of the full HSI image, incorporating as node features the CNN embeddings, the GNN model (each block represents a GAT layer with numbers of input and output channels and attention heads), and the resulting node predictions, which can be directly interpreted as image segmentation result.

ionizing, and label-free, i.e., does not require a contrast agent. The information provided by the spectral properties of biological tissues can be used to distinguish them [30].

HSI has been used on biopsies, histopathological and fluorometric analysis, and disease biology [14,37,43]. In medical computer vision research, it was used for tumor/healthy tissue differentiation of multiple cancer types [11,21,24].

These recent studies relied on the assumption that the spectral domain should contain most of the necessary information for tumor differentiation. Thus, hyperspectral images are decomposed into single pixels or small spatial tiles that are analyzed independently. This has two significant drawbacks: firstly, it destroys any spatial context information, and secondly, the tiles typically have varying data quality, which may bias the results.

Contributions In this work, we present an ML method for overcoming the two aforementioned limitations of the current state of the art. By introducing additional context and application information to the ML model, we improve the prediction quality for the task of tumor/healthy tissue segmentation on unseen samples.

Firstly, we introduce spatial context information to the model by utilizing Graph Neural Networks (GNNs). We

connect hyperspectral tiles based on their spatial proximity into a graph and feed it to a GNN, whereby image segmentation is seen as a graph node classification task. Our novel approach extracts tile-specific features with a CNN encoder and uses them as the node features for the GNN (see Fig. 1). An end-to-end training strategy ensures that task-specific information is extracted simultaneously on various scales, optimally combining spatial and spectral information.

Secondly, we investigate whether the local quality of HSI data influences the segmentation results by changing the training set from only spatially and spectrally homogeneous tiles to all available tiles. We confirm that tiles of a lower quality harm network performance. We then derive a custom loss function that weights the contribution from each spatial tile based on custom quality metrics. Thus, information of the lower-quality data is still used, but it does not contribute as much as good-quality data to the final model.

Our quantitative evaluations show that all GNN models outperform CNN-based counterparts, improving accuracy for all classes. Qualitative results illustrate that predictions from GNN-based models are smoother and do not suffer from isolated classification errors. Furthermore, our novel quality-aware loss function exhibits superior performance compared to the baseline, especially on the tumor class.

The rest of this paper is structured as follows: after discussing related work in Sec. 2, we present our methods in Sec. 3, describe the results in Sec. 4, and conclude in Sec. 5.

2. Related work

Here we first summarize the state of the art of medical HSI data segmentation, then we review GNN applications to medical non-HSI data and to non-medical HSI data. To the best of our knowledge, no previous work used GNNs on medical HSI data.

2.1. Semantic segmentation of medical HSI data

Different methods exist to maximise information extraction for HSI-based tissue segmentation [45]. In the simplest cases, a physical inverse model can be used [34]. More often however, a forward model is lacking, and data-driven ML models are required [20], either classical [2, 40] or based on deep learning [8, 32, 35].

Different strategies are possible for the combinations of spatial and spectral information. The simplest single-pixel classification relies entirely on the spectral domain [2]; alternatively, spectral and spatial domains can be combined, e.g., by engineering spectral-spatial features in classical ML [28]. Most deep learning approaches have been based on multi-channel 2D CNNs, applied independently to macropixels (patches) to improve signal-to-noise and utilize at least part of the spatial information. This was the strategy adopted by the HELICoiD project [12], which developed an intraoperative demonstrator for in vivo brain tumor segmentation for surgical support. Their final dataset consisted of 36 images from 22 glioblastoma patients [13]. A combination of classical and deep learning methods (2D CNNs) based on single pixels and patches achieved accuracies $> 98\%$ [11, 22, 25, 38]; patch-wise fully 3D CNNs were also used [25, 38]. The same patch-based models were used for in vitro segmentation [44] and other medical applications, including H&N cancer (SCC) segmentation [23, 25, 26]. A similar pixel-wise model was applied by Urbanos et al. [59] on an independent HSI brain cancer dataset, and patch-wise using SLIC [1] aggregation by Giannantonio et al. [21] on low-grade glioma data.

While the typical HSI data sizes and data scarcity can make full-image models unwieldy, full-image segmentation approaches were also proposed. Trajanovski et. al [57, 58] segmented an HSI dataset of tongue cancer from 14 patients using U-Net [49] based on patches of size 256×256 . Cervantes et al. [5] segmented HSI data from hepatic (18 images) and thyroid (21 images) surgeries with U-Net on patches of size 8×8 . Garifullin et al. [19] segmented 55 retinal HSI images using SegNet [3] and Dense-FCN [31]. Wang et al. [63] defined the 3D Hyper-Net encoder-decoder model to segment HSI melanoma images. Yun et al. [70] presented the SpecTr Spectral Transformer model, by intro-

ducing a transformer into the encoding part of a U-Net, on a dataset of 514 cholangiocarcinoma HSI images. Seidlitz et al. [52] compared pixel- vs. patch-based vs. full-image organ segmentation on 506 HSI animal images.

2.2. GNN segmentation of medical (non-HSI) data

Graph Neural Networks (GNNs) [6,66] are deep learning models that operate on data in graph form [4]; they have been successfully applied to diverse tasks in recent years, since the introduction of the Graph Convolutional Network model [33] and its later extensions such as GraphSAGE [27] and the Graph Attention Network (GAT) [60].

Any image can be seen as a graph, with the pixels as the nodes and the edges drawn, e.g., to the neighbours. This idea is attractive in case of large medical data, such as HSI but also volumetric data such as MRI or CT scans, which can be first aggregated into super-pixels (-voxels), and then processed as a graph with GNNs. The benefits are twofold: circumventing the cost of processing the raw data cube with CNNs, and incorporating domain knowledge in the definition of nodes and edges.

This approach has been applied to several medical image segmentation task. Yan et al. [67] used GNNs (ChebNets) to segment brain tissue from MRI data. Juarez et al. [18] combined U-Nets with GNNs to segment airways from CT scans. Saueressig et al. [50, 51] performed brain tumor segmentation from MRI images, obtaining best results with GraphSAGE. Duan et al. [10] segmented eye fundus images (RGB) using a combination of CNN and GNN features extracted with a GAT model. Patel et al. [47] also segmented volumetric MRI data using GAT. Gaggion et al. [17] defined the CNN+GNN encoder-decoder model HybridGNet for landmark-based segmentation of chest X-ray data. Shao et al. [56] tracked liver tumor in X-ray data combining GNNs with a biomechanical model.

2.3. GNN segmentation of non-medical HSI data

Outside the medical domain, multiple GNN models have been developed for HSI image segmentation, mostly tailored to remote sensing and land coverage classification.

Qin et al. [48] defined the spectral-spatial GCN that combines spectral and spatial similarity in the edge definition. Shahraki et al. [55] combined a 1D CNN feature extractor with GCNs. Sha et al. [54] employed edge convolutions in semi-supervised mode, while Hong et al. [29] presented the miniGCN model that subdivides nodes in mini-batches. Wan et al. [61] introduced the multi-scale dynamic GCN (MDGCN) model that considers the connection to multi-hop neighbors; later from this model the context-aware dynamic GCN was derived [62], where the adjacency matrix is dynamically refined. Several further variants were introduced [36], including defining a graph over the whole HSI image [41] and using GATs [53, 64] and GraphSAGE [68].

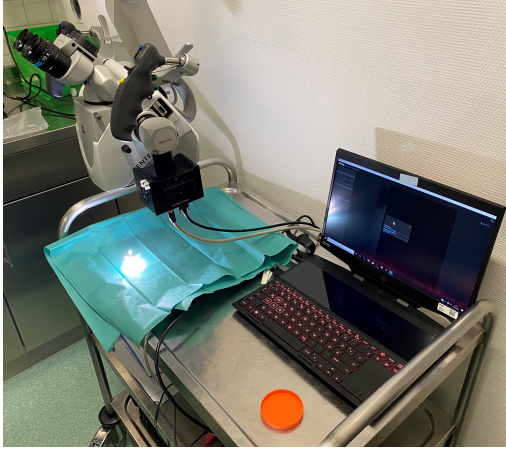


Figure 2. Laboratory setup at the ENT department of University Hospital Ulm: an IMEC HSI snapscan camera connected to a ZEISS OPMI[®] PENTERO[®] microscope for ex vivo HSI and RGB data acquisition.

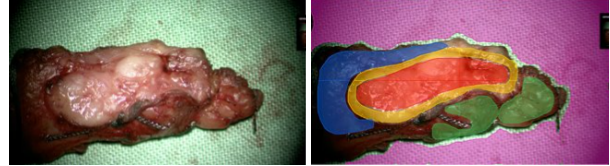
Zhang et al. [71] later introduced the Global Random Graph Convolution Network (GR-GCN), which reduces graph size by random sampling. Ding et al. [9] proposed the multi-scale receptive fields graph attention network (MRGAT), which combines CNNs with GATs on multiple scales. Yao et al. [69] presented a deep hybrid multi-graph neural network (DHMG) that employs a spectral filter to extract features and an auto-regressive average for noise suppression.

3. Methodology

3.1. Data acquisition

We follow the configuration described in Ref. [21] for HSI data acquisition. In brief, ex vivo HSI image acquisition was performed at the ENT department of University Hospital Ulm, employing an IMEC Snapscan VNIR hyperspectral camera in conjunction with a ZEISS OPMI[®] PENTERO[®] 900 surgical microscope through its optical port.

The HSI setup shown in Fig. 2 is prepared before the start of tumor surgery. Following tumor resection, the ex vivo tumor specimen undergoes a saline solution rinse to eliminate residual blood from its surface. Next, the sample is promptly taken to the laboratory-based HSI setup for data acquisition. For each specimen, a minimum of two HSI images are typically captured: an initial panoramic image covering the entire sample area to facilitate subsequent annotation of tissue categories, and an image with a reduced working distance and higher magnification to scrutinize the tumor center and margin in greater detail. A consistent lighting scheme and region of interest are maintained by capturing an RGB photograph prior to each HSI image acquisition using the PENTERO microscope. The selection



(a) RGB image (b) Annotated image

Figure 3. RGB image of one exemplary resected tissue sample (a) and its corresponding labels (b) annotated by medical experts, depicting in red, yellow, blue, green, and magenta the classes tumor, tumor margin, healthy, muscle and background respectively.

of microscope working distance and magnification values is determined based on the dimensions of the respective specimens. A constant light intensity of 50% is used on the PENTERO microscope for all HSI measurements.

Post-operation, surgeons annotate diverse tissue classes within RGB images based on their prior knowledge from pre- and intra-surgical diagnostics. The RGB images and annotations are subsequently registered with their HSI counterparts.

3.2. Data characterization and preparation

Our dataset consists of HSI images of otolaryngological tumor of SCC type. It comprises a total of 51 annotated images from 30 patients with resolution 1600×1600 pixels. We remove two images, as based on medical assessment they were found to display a different tumor type, thus leaving us with 49 images for analysis. Every HSI image has $N_\lambda = 109$ wavelength channels in the visible spectrum between approximately 468 nm – 790 nm. Four classes were annotated by medical experts namely, tumor, tumor margin, healthy and muscle. We additionally annotated a background class using the same tool for extending model robustness. For all experiments, we only consider the three classes tumor, healthy, and background, as the muscle class is poorly sampled and tumor margin has large annotation uncertainty. We show in Fig. 3 one example RGB image and its annotations.

In order to boost signal-to-noise and support the segmentation task, we aggregate pixels into tiles (macro-pixels) by using a modified version of the SLIC algorithm [1], which aggregates pixels to minimize a combination of spatial and color distances between them. We set the color distance to be the Spectral Angle Mapper (SAM) distance, which for two pixels i, j of spectra $\mathbf{s}_i, \mathbf{s}_j$ is given by

$$\text{SAM}(\mathbf{s}_i, \mathbf{s}_j) = \cos^{-1} \left(\frac{\mathbf{s}_i \cdot \mathbf{s}_j}{\|\mathbf{s}_i\| \|\mathbf{s}_j\|} \right). \quad (1)$$

Alternatively, the L_2 distance can be used, as given by

$$L_2(\mathbf{s}_i, \mathbf{s}_j) = \sqrt{\sum_{l=1}^{N_\lambda} (s_{il} - s_{jl})^2}. \quad (2)$$

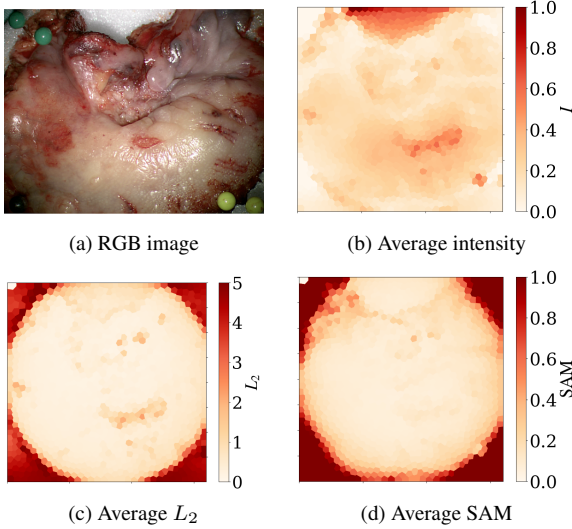


Figure 4. Tile quality metrics of the representative tissue sample shown in panel (a). The remaining panels display the three tile quality metrics we consider: average tile intensity I (panel b), and the average intra-tile spectral distances from the mean L_2 , SAM in panels (c, d) respectively.

We set the number SLIC tiles to contain ~ 200 pixels each.

We consider as possible proxies of each tile’s T_i quality its average pixel intensity I_i (to isolate under-exposed and saturated regions) and the quantities $L_{2,i}$, SAM_i that are obtained by taking the average distances between the spectrum at each pixel $\mathbf{s}_j \forall j \in T_i$ and the tile’s average spectrum $\bar{\mathbf{s}}_i$, i.e., $L_{2,i} \equiv \frac{1}{|T_i|} \sum_{j \in T_i} L_2(\mathbf{s}_j, \bar{\mathbf{s}}_i)$ (large spectral distances indicate low uniformity). (We drop the i indices henceforth for simplicity.) As depicted in Fig. 4, tile quality across an image displays significant variations. Therefore, to build a dataset with only high-quality tiles, we follow the approach by Ref. [21] and discard the tiles that have poor quality by applying threshold cuts on the three mentioned metrics: low spectral uniformity (we discard the upper 75% percentile on both average SAM and L_2), extremely high or low mean intensity (we discard the lowest and highest 10% percentiles in I), as well as tiles with non-uniform class labels. This results in a dataset consisting of high-quality tiles only.

The total amount of tiles in our dataset is 36 693, of which 26 190 are high-quality tiles. We split the data into training+validation and testing samples patient-wise, retaining all images from six patients for testing, i.e., we use 39 images for training and validation and 10 images for testing. We divide accordingly both full and high-quality dataset into three sets containing 65%, 16.5%, and 18.5% of the tiles for the train, val, test respectively.

3.3. Tissue segmentation methods

We consider the two main segmentation methods shown in Fig. 1, CNN-based and CNN+GNN-based, both of which can be extended with our quality-weighted loss function.

CNN method The CNN-based method closely follows the approach of Ref. [21]. Here we isolate the hyperspectral SLIC tiles and spatially zero-pad them to a common shape of $48 \times 48 \times 109$ ($x \times y \times \lambda$), so that they can be passed to a CNN model for classification. We then aggregate the CNN predictions into a composite image segmentation result.

The CNN model uses a similar encoder architecture to Ref. [21]. We first apply a channel compression layer, implemented with a 1×1 convolutional kernel with stride 1 and no padding, to reduce the number of spectral dimensions from $N_\lambda = 109$ to $N_{\text{ch}} = 12$. We then apply four 2D convolutional blocks bringing the number of features from N_{ch} to $(N_f/2, N_f, 2N_f, 4N_f)$ respectively, where we take $N_f = 12$. The kernel sizes are respectively (3, 4, 4, 4), the strides (1, 2, 2, 2) and padding (1, 1, 1, 1). The resulting features of dimensions $48 \times 6 \times 6$ are then average-pooled, thus yielding for each tile i an encoded representation $\mathbf{z}_i \in \mathbb{R}^{48}$, which we pass to a fully connected classification head. We apply a LeakyReLU activation and Batch-Norm after each convolutional layer.

During training we apply the following data augmentation: a 50% dropout before the classification layer, a random shift along spatial axes, a random pixel brightness shift, and random rotation, rescaling, and Gaussian blurring.

Our baseline strategy consists of training only on the high-quality tiles (training and validation splits) obtained with the procedure described in Sec. 3.2, using a regular cross-entropy loss function summed over all tiles. At test time, we always evaluate the model on all annotated image areas (test split, whereby tiles are generated on the test data on the fly, so the exact number will vary).

CNN with quality-weighted loss While the exclusion of low-quality tiles at train time generally makes the models more robust on the good-quality areas, in any realistic surgical setting it would be desirable to have meaningful predictions over the full image, including lower-quality areas.

To address this requirement, we incorporate all tiles to the training and validation sets while introducing a quality-weighted loss function to downweight low-quality tiles. We define the loss weighting factor w_i for each tile T_i as

$$w_i = w_I(I_i) \cdot w_{L_2}(L_{2,i}) \cdot w_{\text{SAM}}(\text{SAM}_i), \quad (3)$$

where the quality metrics I , L_2 , SAM are defined in

Sec. 3.2. We choose for the three components the forms:

$$\begin{aligned}
 w_I(I) &= \begin{cases} 6I & \text{if } I \leq 0.167 \\ 1 & \text{if } 0.167 < I < 0.5 \\ 2 - 2I & \text{if } I \geq 0.5 \end{cases} \\
 w_{L_2}(L_2) &= 0.7^{L_2} \\
 w_{\text{SAM}}(\text{SAM}) &= 0.4^{\text{SAM}}. \tag{4}
 \end{aligned}$$

With this strategy, the model during training also uses the low-quality tiles, albeit with less weight, so that information from those regions is not lost. At test time, we expect better generalization, especially in the regions with high density of blood vessels, low light, and close to saturated areas.

We compare the results obtained by training on all tiles with the weighted loss with the model trained on good tiles only, as well as with the same model trained on all tiles with a regular cross-entropy loss.

CNN + GNN method We improve over the CNN baseline by incorporating the spatial context of the tiles using GNNs. For every HSI image, we construct an undirected graph $\mathcal{G} = (\mathcal{V}, \mathcal{E})$ with vertices \mathcal{V} and edges \mathcal{E} . Here $N = |\mathcal{V}|$ is the number of nodes, and $A \in \mathbb{R}^{N \times N}$ is the adjacency matrix. In this context, the vertices represent the tiles, and the edges their relational structure.

In order to characterize the nodes, we need to aggregate the tiles’ spectral information into a matrix $X \in \mathbb{R}^{N \times F}$, where F is the dimensionality of the aggregated features per tile. To encode intra-tile structure in both spatial and spectral domains, we choose to use our baseline CNN model as a feature extractor, thus setting $X = Z \in \mathbb{R}^{N \times 48}$, where we aggregate the latent space representation of all tiles into one matrix Z . Differently from the baseline CNN model, in this case we do not apply batch normalization to the CNN, and we use for the final dropout layer of the CNN model a 30% probability, as the GNN is less prone to overfitting.

We define the adjacency matrix A by simply selecting for each tile its k nearest neighbors with a kNN algorithm, using $k = 2$; we find this small number of neighbors to be effective in combating overfitting, which we observed in increasing amounts for $k \in \{3, 5\}$.

The graphs thus defined are then passed to a Graph Attention Network (GAT) [60] with 64 hidden channels, 3 hidden GAT layer and 3 attention heads. After each GAT layer, a ReLU activation is applied, and before the last layer we apply a 30% dropout during training. While we experimented with different GNN choices, we found the GAT model to be suitable for our use-case as opposed to simpler graph-convolutional layers such as the GCN [33]. The attention mechanism provides the flexibility of applying different weights for different nodes in each tile’s neighborhood, which is likely to be beneficial, e.g., near tissue class

boundary regions. We note however that a full optimization of the GNN architecture is beyond the scope of this work.

During training, in addition to the CNN-level augmentation described above, we apply graph-level data augmentation by randomly jittering the spatial coordinates associated with each and by randomly dropping up to 30% of the nodes. We use per-node cross-entropy as the loss function. While it is possible to train the CNN+GNN model end-to-end in principle, we found that in order to reduce overfitting, it is beneficial to not let gradients flow from the GNN head into the CNN backbone during backpropagation, and instead minimize the combined loss $L_{\text{comb}} = L_{\text{CNN}} + L_{\text{GNN}}$, where both losses are cross-entropy.

As for the CNN case, our baseline strategy is to first train the model using graphs constructed from the good-quality tiles only; at test time we always evaluate the model on all annotated image areas of the 10 left-out images. Then we include all tiles in the training by introducing the quality-weighted loss. Also here, we will compare the results obtained by training on graphs constructed from all tiles using weighted and unweighted losses with the baseline model trained on graphs constructed from good tiles only.

4. Results

We trained all models described in Sec. 3.3 on a Linux machine with 12 CPU cores, 64 GB RAM, and an NVIDIA GeForce RTX™ 3090 GPU (24 GB RAM).

4.1. Quantitative evaluation

We summarize in Tab. 1 the quantitative results of all experiments described in Sec. 3.3 and evaluated on the test set that includes all annotated image areas. Here we report the accuracy, F_1 -score and IoU [42] metrics per class (H, T, B for healthy, tumor, and background respectively) and macro-averaged across all classes. Additionally, we report the integrated area under the ROC curve (AUC) for the tumor/healthy binary classification problem, where we excluded the background class, since it is irrelevant for the clinical application. The ROC curves for all models are shown in Fig. 5.

In the analysis of the results, the closest previous work we can compare to is the method by Ref. [21], which is equivalent to our CNN_g model. Other CNN-based models build on top of the baseline CNN_g model.

While the CNN models already reach nontrivial accuracy, surpassing 80% in most cases, the GNN method leads to an overall superior performance. All best results of Tab. 1 lie in the GNN section, and a like-to-like comparison shows that the GNN approach improves average accuracy by 11 percent points (pp) for training on good-quality tiles compared to the CNN_g baseline, by 1 pp for all tiles, and by 2 pp in the weighted loss case.

Table 1. Quantitative comparison of model performance. We report accuracy, F_1 -score, and IoU on each class (H, T, B refer to healthy, tumor and background respectively) and macro-averaged across all classes (Avg); additionally, we also report the ROC AUC for the healthy/tumor binary classification task. The top half refers to the CNN-only method, the bottom half describes the CNN+GNN method. Models trained on good tiles only, on all tiles, and on all tiles with a quality-weighted loss are denoted with $_g$, $_a$, $_aW$ respectively. The best results for each class are presented in bold. The CNN $_g$ model is equivalent to Ref. [21].

Model	Accuracy				F_1 -score				IoU				AUC
	H	T	B	Avg.	H	T	B	Avg.	H	T	B	Avg.	H vs. T
CNN $_g$ [21]	0.83	0.68	0.86	0.79	0.79	0.63	0.83	0.75	0.68	0.48	0.75	0.64	0.86
CNN $_a$	0.85	0.76	0.94	0.85	0.82	0.69	0.92	0.81	0.71	0.56	0.71	0.66	0.88
CNN $_aW$	0.84	0.80	0.97	0.87	0.85	0.71	0.88	0.81	0.74	0.58	0.73	0.68	0.91
GNN $_g$	0.78	0.92	1.00	0.90	0.84	0.77	0.91	0.84	0.73	0.65	0.78	0.72	0.92
GNN $_a$	0.94	0.64	0.99	0.86	0.85	0.67	0.99	0.84	0.75	0.50	0.84	0.69	0.92
GNN $_aW$	0.87	0.83	0.98	0.89	0.87	0.74	0.95	0.85	0.78	0.60	0.82	0.73	0.95

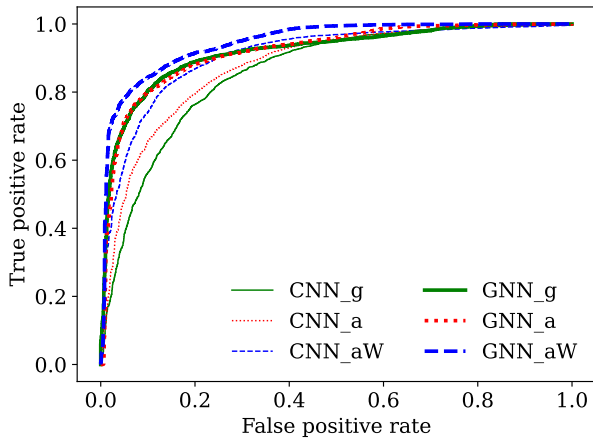


Figure 5. ROC curves for each model for the binary tumor/healthy classification task (background class was removed). The thick lines corresponding to GNN models are always above the thin lines describing their CNN counterparts. While the training on all tiles ($_a$ models) with unweighted loss is not always beneficial, the inclusion of a weighted loss ($_aW$ models) yields a significant improvement in all cases. The CNN $_g$ model corresponds to the approach by Ref. [21].

Models trained on all tiles without weighted loss function yield contradicting results: they show a better performance on the healthy class, but in some cases yield degraded results on the tumor class. This behaviour can be explained by the decreased quality of the dataset, where individual tiles contain heterogeneous spectral information and suffer from high noise and signal saturation. The introduction of a weighted loss improves the results compared to the use of all tiles without weights, by rebalancing the performance between classes. The healthy class quality decreases, while the tumor class quality increases, leading to an average accuracy improvement of 2 pp (3 pp) for the

CNN (GNN) methods. Quantitative results according to the different metrics are largely consistent: GNN methods are superior, and the usage of a weighted loss improves most metrics, although from the point of view of a correct detection of the tumor class, the GNN model trained on good tiles only is ahead.

The ROC curve of Fig. 5, together with the reported AUC, provides a good single-number summary of each model quality for clinical applications. We observe once again that the GNN models are superior, that the addition of a weighted loss is beneficial, and specifically that each GNN model is ahead of its CNN counterpart. Our best model, GNN $_aW$, is according to this metric 9 percent points ahead of the baseline from Ref. [21], CNN $_g$, with an evident gap across all threshold levels in the ROC curve.

4.2. Qualitative evaluation

We next compare the results qualitatively on four representative images from the test set in Fig. 6. We show for each example the ground truth followed by the segmentation predictions using each of the models of Tab. 1.

Both CNN and GNN models succeed in producing a qualitatively correct result in most cases, such as the first three examples. The last example is a more challenging sample, where we observe a substantial fraction of false positives, which are however reduced when using more advanced approaches (columns d, g). For all example results, the CNN models (columns b-d) are as expected noisier, as they cannot make use of contextual information. The GNN models (columns e-g), on the contrary, leverage context to achieve a smoother prediction.

Models trained on good tiles only (columns b, e) feature as expected a high error rate on lower-quality areas that were not seen during training, e.g., in over-/under-exposed patches and in noisy areas. As also seen quantitatively in Tab. 1, GNN models trained on all tiles (column f) display a degraded performance on the tumor class prediction. A

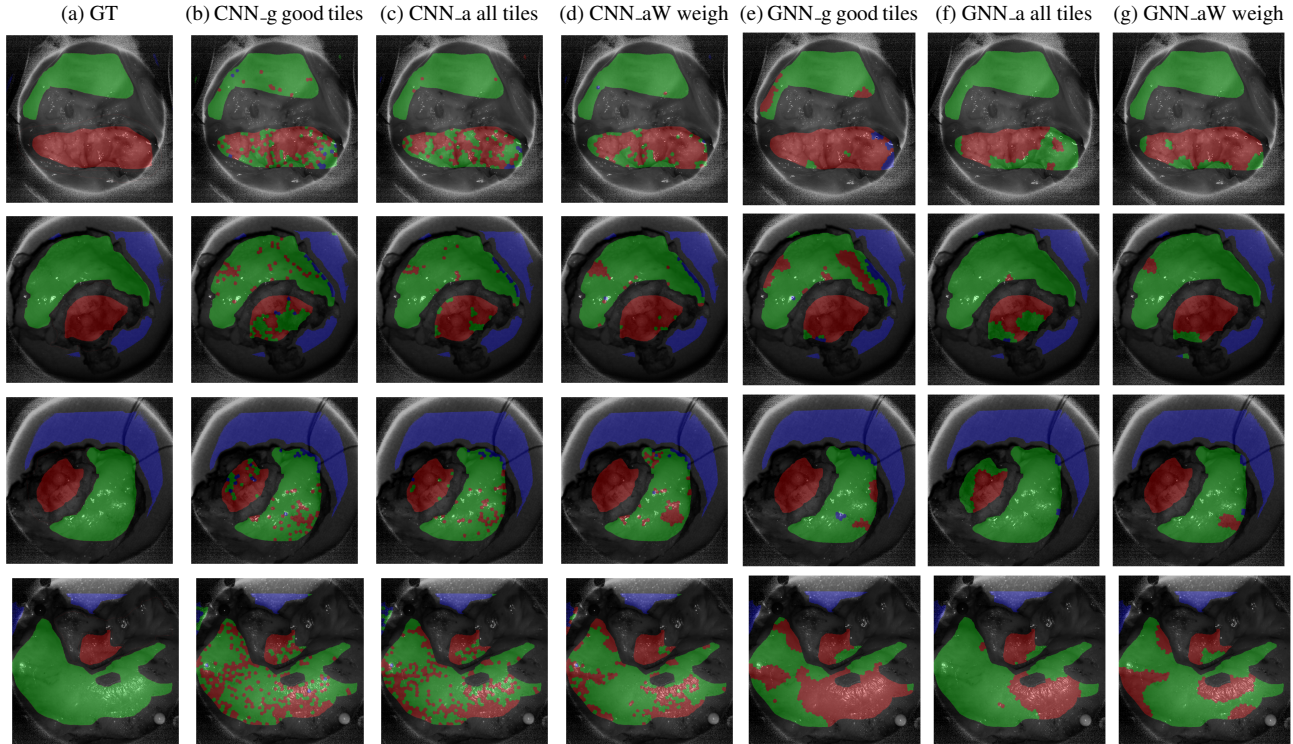


Figure 6. Qualitative comparison of the inference results on the test set for the different approaches described in Sec. 3.3 and quantitatively summarized in Tab. 1. Each row shows the inference on one test example; column (a) shows the ground truth, and the remaining columns display the results with each model. The grayscale images in the background represent luminosity in an intermediate wavelength channels for illustration, and the overlaid colors indicate the tissue classes: red, green and blue denote tumor, healthy and background respectively.

more robust prediction of this class is then restored once the weighted loss is introduced (columns d, g for CNN and GNN respectively). The qualitative evaluation confirms that our best model, GNN_aW, brings a significant improvement compared with the baseline from Ref. [21], CNN_g.

5. Conclusions and future work

In this work, we presented a novel approach for HSI-based tumor segmentation that leverages recent advances in the field of Graph Neural Networks (GNNs) to fully exploit HSI information in both spectral and spatial domains. We used for the first time a composite CNN+GNN model for tile-based medical HSI image segmentation. After the creation of macropixels (tiles) with an adapted version of the SLIC algorithm [1], we defined for each HSI image a graph object whose nodes are the tiles and whose edges connect neighboring tiles. The node features are defined by applying a CNN feature extractor to the tile data cube, thus maximizing the extraction of intra-tile spatial and spectral information. Global spatial information is in turn optimally used by passing the graph through a GAT [60] graph model for node classification.

We evaluated this approach on a dataset of 51 HSI ex

vivo images from 30 patients. We compared the segmentation results of the GNN models with a baseline CNN by Ref. [21]. We additionally introduced a loss weighting scheme based on local image quality that aims at recovering good segmentation results also on lower-quality regions.

We found that all models, including the CNN baseline from Ref. [21], achieved good accuracy ($> 80\%$) on a test dataset consisting of images from unseen patients. However, as expected, GNN models do make better use of spatial information, thus leading to more accurate and uniform results compared with the baseline: for models trained on good-quality image regions only, GNNs improved the average accuracy with respect to the baseline from 79% to 90%; a qualitative analysis also confirmed the superior performance and better spatial uniformity of the GNN results.

We also demonstrated that our new quality-aware loss weighting scheme improves the robustness of the predictions for both CNN and GNN models: the average accuracy of CNN models improves from 79% to 87% with the weighted loss, and while the overall average accuracy of GNN models does not improve, its F_1 -score does, as well as its qualitative spatial uniformity.

Our work shows that GNNs together with a quality-

aware loss weighting strategy lead to robust tissue segmentation that generalizes to unseen patients. The next step for future research will be to apply this method to in vivo and intra-operative settings, thus paving the way for improved surgery workflow and patient outcome.

References

- [1] Radhakrishna Achanta, Appu Shaji, Kevin Smith, Aurelien Lucchi, Pascal Fua, and Sabine Süsstrunk. Slic superpixels compared to state-of-the-art superpixel methods. *IEEE transactions on pattern analysis and machine intelligence*, 34(11):2274–2282, 2012. [3](#), [4](#), [8](#)
- [2] Hamed Akbari, Yukio Kosugi, Kazuyuki Kojima, and Naofumi Tanaka. Wavelet-based compression and segmentation of hyperspectral images in surgery. In *Medical Imaging and Augmented Reality: 4th International Workshop Tokyo, Japan, August 1-2, 2008 Proceedings 4*, pages 142–149. Springer, 2008. [3](#)
- [3] Vijay Badrinarayanan, Alex Kendall, and Roberto Cipolla. Segnet: A deep convolutional encoder-decoder architecture for image segmentation. *IEEE transactions on pattern analysis and machine intelligence*, 39(12):2481–2495, 2017. [3](#)
- [4] John Adrian Bondy. *Graph theory with applications*. 1982. [3](#)
- [5] Fernando Cervantes-Sanchez, Marianne Maktabi, Hannes Köhler, Robert Sucher, Nada Rayes, Juan Gabriel Avina-Cervantes, Ivan Cruz-Aceves, and Claire Chalopin. Automatic tissue segmentation of hyperspectral images in liver and head neck surgeries using machine learning. *Artif Intell Surg*, 1:22–37, 2021. [3](#)
- [6] Xiaojun Chang, Pengzhen Ren, Pengfei Xu, Zhihui Li, Xiaojiang Chen, and Alex Hauptmann. A comprehensive survey of scene graphs: Generation and application. *IEEE Transactions on Pattern Analysis and Machine Intelligence*, 45(1):1–26, 2021. [3](#)
- [7] Neil T Clancy, Geoffrey Jones, Lena Maier-Hein, Daniel S Elson, and Danail Stoyanov. Surgical spectral imaging. *Medical image analysis*, 63:101699, 2020. [1](#)
- [8] Rong Cui, He Yu, Tingfa Xu, Xiaoxue Xing, Xiaorui Cao, Kang Yan, and Jiexi Chen. Deep learning in medical hyperspectral images: A review. *Sensors*, 22(24):9790, 2022. [3](#)
- [9] Yao Ding, Zhili Zhang, Xiaofeng Zhao, Danfeng Hong, Wei Cai, Nengjun Yang, and Bei Wang. Multi-scale receptive fields: Graph attention neural network for hyperspectral image classification. *Expert Systems with Applications*, 223:119858, 2023. [4](#)
- [10] Sixu Duan, Pu Huang, Min Chen, Ting Wang, Xiaolei Sun, Meirong Chen, Xueyuan Dong, Zekun Jiang, and Dengwang Li. Semi-supervised classification of fundus images combined with cnn and gc. *Journal of Applied Clinical Medical Physics*, 23(12):e13746, 2022. [3](#)
- [11] Himar Fabelo, Martin Halicek, Samuel Ortega, Maysam Shahedi, Adam Szolna, Juan F Piñeiro, Coralía Sosa, Aruma J O’Shanahan, Sara Bisshopp, Carlos Espino, et al. Deep learning-based framework for in vivo identification of glioblastoma tumor using hyperspectral images of human brain. *Sensors*, 19(4):920, 2019. [2](#), [3](#)
- [12] Himar Fabelo, Samuel Ortega, Silvester Kabwama, Gustavo M Callico, Diederik Bulters, Adam Szolna, Juan F Pineiro, and Roberto Sarmiento. Helicoid project: A new use of hyperspectral imaging for brain cancer detection in real-time during neurosurgical operations. In *Hyperspectral Imaging Sensors: Innovative Applications and Sensor Standards 2016*, volume 9860, page 986002. SPIE, 2016. [3](#)
- [13] Himar Fabelo, Samuel Ortega, Adam Szolna, Diederik Bulters, Juan F Piñeiro, Silvester Kabwama, Aruma JO’Shanahan, Harry Bulstrode, Sara Bisshopp, B Ravi Kiran, et al. In-vivo hyperspectral human brain image database for brain cancer detection. *IEEE Access*, 7:39098–39116, 2019. [3](#)
- [14] Baowei Fei. Hyperspectral imaging in medical applications. In *Data Handling in Science and Technology*, volume 32, pages 523–565. Elsevier, 2020. [2](#)
- [15] Jacques Ferlay, Isabelle Soerjomataram, Rajesh Dikshit, Sultan Eser, Colin Mathers, Marise Rebelo, Donald Maxwell Parkin, David Forman, and Freddie Bray. Cancer incidence and mortality worldwide: sources, methods and major patterns in globocan 2012. *International journal of cancer*, 136(5):E359–E386, 2015. [1](#)
- [16] Miranda M Fidler, Freddie Bray, Salvatore Vaccarella, and Isabelle Soerjomataram. Assessing global transitions in human development and colorectal cancer incidence. *International journal of cancer*, 140(12):2709–2715, 2017. [1](#)
- [17] Nicolás Gaggion, Lucas Mansilla, Candelaria Mosquera, Diego H Milone, and Enzo Ferrante. Improving anatomical plausibility in medical image segmentation via hybrid graph neural networks: applications to chest x-ray analysis. *IEEE Transactions on Medical Imaging*, 42(2):546–556, 2022. [3](#)
- [18] Antonio Garcia-Uceda Juarez, Raghavendra Selvan, Zaigham Saghir, and Marleen de Bruijne. A joint 3d unet-graph neural network-based method for airway segmentation from chest cts. In *Machine Learning in Medical Imaging: 10th International Workshop, MLMI 2019, Held in Conjunction with MICCAI 2019, Shenzhen, China, October 13, 2019, Proceedings 10*, pages 583–591. Springer, 2019. [3](#)
- [19] Azat Garifullin, Peeter Kõöbi, Pasi Ylitepsa, Kati Ådjers, Markku Hauta-Kasari, Hannu Uusitalo, and Lasse Lensu. Hyperspectral image segmentation of retinal vasculature, optic disc and macula. In *2018 Digital Image Computing: Techniques and Applications (DICTA)*, pages 1–5. IEEE, 2018. [3](#)
- [20] Pedram Ghamisi, Javier Plaza, Yushi Chen, Jun Li, and Antonio J Plaza. Advanced spectral classifiers for hyperspectral images: A review. *IEEE Geoscience and Remote Sensing Magazine*, 5(1):8–32, 2017. [3](#)
- [21] Tommaso Giannantonio, Anna Alperovich, Piercosimo Semeraro, Manfredo Atzori, Xiaohan Zhang, Christoph Hauger, Alexander Freytag, Siri Luthman, Roeland Vandebriel, Murali Jayapala, et al. Intra-operative brain tumor detection with deep learning-optimized hyperspectral imaging. In *Optical Biopsy XXI: Toward Real-Time Spectroscopic Imaging and Diagnosis*, volume 12373, pages 74–92. SPIE, 2023. [2](#), [3](#), [4](#), [5](#), [6](#), [7](#), [8](#)
- [22] Martin Halicek, James D Dormer, James V Little, Amy Y Chen, and Baowei Fei. Tumor detection of the thyroid and

- salivary glands using hyperspectral imaging and deep learning. *Biomedical Optics Express*, 11(3):1383–1400, 2020. 3
- [23] Martin Halicek, James D Dormer, James V Little, Amy Y Chen, Larry Myers, Baran D Sumer, and Baowei Fei. Hyperspectral imaging of head and neck squamous cell carcinoma for cancer margin detection in surgical specimens from 102 patients using deep learning. *Cancers*, 11(9):1367, 2019. 3
- [24] Martin Halicek, Himar Fabelo, Samuel Ortega, Gustavo M Callico, and Baowei Fei. In-vivo and ex-vivo tissue analysis through hyperspectral imaging techniques: revealing the invisible features of cancer. *Cancers*, 11(6):756, 2019. 2
- [25] Martin Halicek, James V Little, Xu Wang, Mihir Patel, Christopher C Griffith, Amy Y Chen, and Baowei Fei. Tumor margin classification of head and neck cancer using hyperspectral imaging and convolutional neural networks. In *Medical Imaging 2018: Image-Guided Procedures, Robotic Interventions, and Modeling*, volume 10576, pages 17–27. SPIE, 2018. 3
- [26] Martin Halicek, Guolan Lu, James V Little, Xu Wang, Mihir Patel, Christopher C Griffith, Mark W El-Deiry, Amy Y Chen, and Baowei Fei. Deep convolutional neural networks for classifying head and neck cancer using hyperspectral imaging. *Journal of biomedical optics*, 22(6):060503–060503, 2017. 3
- [27] Will Hamilton, Zhitao Ying, and Jure Leskovec. Inductive representation learning on large graphs. *Advances in neural information processing systems*, 30, 2017. 3
- [28] Lin He, Jun Li, Chenying Liu, and Shutao Li. Recent advances on spectral–spatial hyperspectral image classification: An overview and new guidelines. *IEEE Transactions on Geoscience and Remote Sensing*, 56(3):1579–1597, 2017. 3
- [29] Danfeng Hong, Lianru Gao, Jing Yao, Bing Zhang, Antonio Plaza, and Jocelyn Chanussot. Graph convolutional networks for hyperspectral image classification. *IEEE Transactions on Geoscience and Remote Sensing*, 59(7):5966–5978, 2020. 3
- [30] Steven L Jacques. Optical properties of biological tissues: a review. *Physics in Medicine & Biology*, 58(11):R37, 2013. 2
- [31] Simon Jégou, Michal Drozdal, David Vazquez, Adriana Romero, and Yoshua Bengio. The one hundred layers tiramisu: Fully convolutional densenets for semantic segmentation. In *Proceedings of the IEEE conference on computer vision and pattern recognition workshops*, pages 11–19, 2017. 3
- [32] Uzair Khan, Sidike Paheding, Colin P Elkin, and Vijaya Kumar Devabhaktuni. Trends in deep learning for medical hyperspectral image analysis. *IEEE Access*, 9:79534–79548, 2021. 3
- [33] Thomas N Kipf and Max Welling. Semi-supervised classification with graph convolutional networks. *arXiv preprint arXiv:1609.02907*, 2016. 3, 6
- [34] Raquel Leon, Sofia H Gelado, Himar Fabelo, Samuel Ortega, Laura Quintana, Adam Szolna, Juan F Piñeiro, Francisco Balea-Fernandez, Jesus Morera, Bernardino Clavo, et al. Hyperspectral imaging for in-vivo/ex-vivo tissue analysis of human brain cancer. In *Medical Imaging 2022: Image-Guided Procedures, Robotic Interventions, and Modeling*, volume 12034, pages 525–534. SPIE, 2022. 3
- [35] Shutao Li, Weiwei Song, Leyuan Fang, Yushi Chen, Pedram Ghamisi, and Jon Atli Benediktsson. Deep learning for hyperspectral image classification: An overview. *IEEE Transactions on Geoscience and Remote Sensing*, 57(9):6690–6709, 2019. 3
- [36] Bing Liu, Kuiliang Gao, Anzhu Yu, Wenyue Guo, Ruirui Wang, and Xibing Zuo. Semisupervised graph convolutional network for hyperspectral image classification. *Journal of Applied Remote Sensing*, 14(2):026516–026516, 2020. 3
- [37] Guolan Lu and Baowei Fei. Medical hyperspectral imaging: a review. *Journal of biomedical optics*, 19(1):010901–010901, 2014. 1, 2
- [38] Francesca Manni, Fons van der Sommen, Himar Fabelo, Svitlana Zinger, Caifeng Shan, Erik Edström, Adrian Elmi-Terander, Samuel Ortega, Gustavo Marrero Callicó, and Peter HN de With. Hyperspectral imaging for glioblastoma surgery: Improving tumor identification using a deep spectral-spatial approach. *Sensors*, 20(23):6955, 2020. 3
- [39] Shanthi Marur and Arlene A Forastiere. Head and neck squamous cell carcinoma: update on epidemiology, diagnosis, and treatment. In *Mayo Clinic Proceedings*, volume 91, pages 386–396. Elsevier, 2016. 1
- [40] Sara Moccia, Sebastian J Wirkert, Hannes Kenngott, Anant S Vemuri, Martin Apitz, Benjamin Mayer, Elena De Momi, Leonardo S Mattos, and Lena Maier-Hein. Uncertainty-aware organ classification for surgical data science applications in laparoscopy. *IEEE Transactions on Biomedical Engineering*, 65(11):2649–2659, 2018. 3
- [41] Lichao Mou, Xiaoqiang Lu, Xuelong Li, and Xiao Xiang Zhu. Nonlocal graph convolutional networks for hyperspectral image classification. *IEEE Transactions on Geoscience and Remote Sensing*, 58(12):8246–8257, 2020. 3
- [42] Dominik Müller, Iñaki Soto-Rey, and Frank Kramer. Towards a guideline for evaluation metrics in medical image segmentation. *BMC Research Notes*, 15(1):1–8, 2022. 6
- [43] Samuel Ortega, Martin Halicek, Himar Fabelo, Gustavo M Callico, and Baowei Fei. Hyperspectral and multispectral imaging in digital and computational pathology: a systematic review. *Biomedical Optics Express*, 11(6):3195–3233, 2020. 2
- [44] Samuel Ortega, Martin Halicek, Himar Fabelo, Rafael Camacho, María de la Luz Plaza, Fred Godtliebsen, Gustavo M. Callicó, and Baowei Fei. Hyperspectral imaging for the detection of glioblastoma tumor cells in h&e slides using convolutional neural networks. *Sensors*, 20(7):1911, 2020. 3
- [45] Samuel Ortega, Martin Halicek, Himar Fabelo, Eduardo Quevedo, Baowei Fei, and Gustavo Marrero Callico. Information extraction techniques in hyperspectral imaging biomedical applications. In *Multimedia Information Retrieval*. IntechOpen, 2020. 3
- [46] D Max Parkin, Freddie Bray, J Ferlay, and Paola Pisani. Global cancer statistics, 2002. *CA: a cancer journal for clinicians*, 55(2):74–108, 2005. 1
- [47] Dhruvil Patel, Dhruv Patel, Rudra Saxena, and Thangarajah Akilan. Multi-class brain tumor segmentation using graph attention network. *arXiv preprint arXiv:2302.05598*, 2023. 3

- [48] Anyong Qin, Zhaowei Shang, Jinyu Tian, Yulong Wang, Taiping Zhang, and Yuan Yan Tang. Spectral–spatial graph convolutional networks for semisupervised hyperspectral image classification. *IEEE Geoscience and Remote Sensing Letters*, 16(2):241–245, 2018. 3
- [49] Olaf Ronneberger, Philipp Fischer, and Thomas Brox. U-net: Convolutional networks for biomedical image segmentation. In *Medical Image Computing and Computer-Assisted Intervention–MICCAI 2015: 18th International Conference, Munich, Germany, October 5–9, 2015, Proceedings, Part III 18*, pages 234–241. Springer, 2015. 3
- [50] Camillo Saueressig, Adam Berkley, Elliot Kang, Reshma Munbodh, and Ritambhara Singh. Exploring graph-based neural networks for automatic brain tumor segmentation. In *From Data to Models and Back: 9th International Symposium, DataMod 2020, Virtual Event, October 20, 2020, Revised Selected Papers 9*, pages 18–37. Springer, 2021. 3
- [51] Camillo Saueressig, Adam Berkley, Reshma Munbodh, and Ritambhara Singh. A joint graph and image convolution network for automatic brain tumor segmentation. In *International MICCAI Brainlesion Workshop*, pages 356–365. Springer, 2021. 3
- [52] Silvia Seidlitz, Jan Sellner, Jan Odenthal, Berkin Özdemir, Alexander Studier-Fischer, Samuel Knödler, Leonardo Ayala, Tim J Adler, Hannes G Kenngott, Minu Tizabi, et al. Robust deep learning-based semantic organ segmentation in hyperspectral images. *Medical Image Analysis*, 80:102488, 2022. 3
- [53] Anshu Sha, Bin Wang, Xiaofeng Wu, and Liming Zhang. Semisupervised classification for hyperspectral images using graph attention networks. *IEEE Geoscience and Remote Sensing Letters*, 18(1):157–161, 2020. 3
- [54] Anshu Sha, Bin Wang, Xiaofeng Wu, Liming Zhang, Bo Hu, and Jian Qiu Zhang. Semi-supervised classification for hyperspectral images using edge-conditioned graph convolutional networks. In *IGARSS 2019-2019 IEEE International Geoscience and Remote Sensing Symposium*, pages 2690–2693. IEEE, 2019. 3
- [55] Farideh Foroozandeh Shahraki and Saurabh Prasad. Graph convolutional neural networks for hyperspectral data classification. In *2018 IEEE global conference on signal and information processing (GlobalSIP)*, pages 968–972. IEEE, 2018. 3
- [56] Hua-Chieh Shao, Jing Wang, Ti Bai, Jaehee Chun, Justin C Park, Steve Jiang, and You Zhang. Real-time liver tumor localization via a single x-ray projection using deep graph neural network-assisted biomechanical modeling. *Physics in Medicine & Biology*, 67(11):115009, 2022. 3
- [57] Stojan Trajanovski, Caifeng Shan, Pim JC Weijtmans, Susan G Brouwer de Koning, and Theo JM Ruers. Tumor semantic segmentation in hyperspectral images using deep learning. In *International Conference on Medical Imaging with Deep Learning–Extended Abstract Track*, 2019. 3
- [58] Stojan Trajanovski, Caifeng Shan, Pim JC Weijtmans, Susan G Brouwer de Koning, and Theo JM Ruers. Tongue tumor detection in hyperspectral images using deep learning semantic segmentation. *IEEE transactions on biomedical engineering*, 68(4):1330–1340, 2020. 3
- [59] Gemma Urbanos, Alberto Martín, Guillermo Vázquez, Marta Villanueva, Manuel Villa, Luis Jimenez-Roldan, Miguel Chavarrías, Alfonso Lagares, Eduardo Juárez, and César Sanz. Supervised machine learning methods and hyperspectral imaging techniques jointly applied for brain cancer classification. *Sensors*, 21(11):3827, 2021. 3
- [60] Petar Veličković, Guillem Cucurull, Arantxa Casanova, Adriana Romero, Pietro Lio, and Yoshua Bengio. Graph attention networks. *arXiv preprint arXiv:1710.10903*, 2017. 3, 6, 8
- [61] Sheng Wan, Chen Gong, Ping Zhong, Bo Du, Lefei Zhang, and Jian Yang. Multiscale dynamic graph convolutional network for hyperspectral image classification. *IEEE Transactions on Geoscience and Remote Sensing*, 58(5):3162–3177, 2019. 3
- [62] Sheng Wan, Chen Gong, Ping Zhong, Shirui Pan, Guangyu Li, and Jian Yang. Hyperspectral image classification with context-aware dynamic graph convolutional network. *IEEE Transactions on Geoscience and Remote Sensing*, 59(1):597–612, 2020. 3
- [63] Qian Wang, Li Sun, Yan Wang, Mei Zhou, Menghan Hu, Jiangang Chen, Ying Wen, and Qingli Li. Identification of melanoma from hyperspectral pathology image using 3d convolutional networks. *IEEE Transactions on Medical Imaging*, 40(1):218–227, 2020. 3
- [64] Tinghuai Wang, Guangming Wang, Kuan Eeik Tan, and Donghui Tan. Spectral pyramid graph attention network for hyperspectral image classification. *arXiv preprint arXiv:2001.07108*, 2020. 3
- [65] Xi Wang and Bin-bin Li. Deep learning in head and neck tumor multiomics diagnosis and analysis: review of the literature. *Frontiers in Genetics*, 12:624820, 2021. 1
- [66] Zonghan Wu, Shirui Pan, Fengwen Chen, Guodong Long, Chengqi Zhang, and S Yu Philip. A comprehensive survey on graph neural networks. *IEEE transactions on neural networks and learning systems*, 32(1):4–24, 2020. 3
- [67] Zhang Yan, Kong Youyong, Wu Jiasong, Gouenou Coatrieux, and Shu Huazhong. Brain tissue segmentation based on graph convolutional networks. In *2019 IEEE International Conference on Image Processing (ICIP)*, pages 1470–1474. IEEE, 2019. 3
- [68] Pan Yang, Lei Tong, Bin Qian, Zheng Gao, Jing Yu, and Chuangbai Xiao. Hyperspectral image classification with spectral and spatial graph using inductive representation learning network. *IEEE Journal of Selected Topics in Applied Earth Observations and Remote Sensing*, 14:791–800, 2020. 3
- [69] Ding Yao, Zhang Zhi-li, Zhao Xiao-feng, Cai Wei, He Fang, Cai Yao-ming, and Wei-Wei Cai. Deep hybrid: multi-graph neural network collaboration for hyperspectral image classification. *Defence Technology*, 23:164–176, 2023. 4
- [70] Boxiang Yun, Yan Wang, Jieneng Chen, Huiyu Wang, Wei Shen, and Qingli Li. Spectr: Spectral transformer for hyperspectral pathology image segmentation. *arXiv preprint arXiv:2103.03604*, 2021. 3
- [71] Chaozi Zhang, Jianli Wang, and Kainan Yao. Global random graph convolution network for hyperspectral image classification. *Remote Sensing*, 13(12):2285, 2021. 4